FULL PAPER

Unraveling the Complex Nanomorphology of Ternary Organic Solar Cells with Multimodal Analytical Transmission Electron Microscopy

Stefanie Rechberger,* Nicola Gasparini, Ranbir Singh, Min Kim, Christos L. Chochos, Vasilis G. Gregoriou, Kilwon Cho, Christoph J. Brabec, Tayebeh Ameri,* and Erdmann Spiecker*

Elucidating the complex materials distribution in the active layers of ternary organic solar cells is one of the greatest challenges in the field of organic photovoltaics. Knowledge of the nanomorphology is key to understanding photophysical processes (e.g., charge separation, adjustment of the recombination mechanism, and suppression of the radiationless and energetic losses) and thus improving the device performance. Herein, for the first time, the successful discrimination and spatial mapping of the active layer components of a ternary organic solar cell are demonstrated using analytical transmission electron microscopy. The material distribution of all three organic components is successfully visualized by multimodal imaging using complementary electron energy loss signals. A complete picture of the morphological aspects can be gained by studying the lateral and cross-sectional morphology as well as the morphology evolution as a function of the mixing ratio of the polymers. Finally, a correlation between the morphology, photophysical processes, and device performance of the ternary and the reference binary system is achieved, explaining the differences of the power conversion efficiency between the two systems.

1. Introduction

Significant improvement of the device performance of organic photovoltaics (OPV) could be achieved in recent years using novel materials and adapted device engineering.[1] However, the power conversion efficiency (PCE) of OPV still lacks behind the inorganic counterparts, such as silicon and perovskite solar cells. One of the main limitations of organic materials (polymers and small molecules) is the narrow absorption band that limits the light-to-current conversion. In recent years, one of the leading strategies to extend the spectral absorption of organic materials is the concept of ternary organic bulk heterojunction (BHJ) solar cells.[2] Ternary blends typically comprise two organic electron donor materials, which absorb light in different wavelength ranges to better match the solar spectrum

Dr. S. Rechberger, Prof. E. Spiecker
Institute of Micro- and Nanostructure Research
Center for Nanoanalysis and Electron Microscopy
Friedrich-Alexander University Erlangen-Nuremberg
Cauerstraße 3, 91058 Erlangen, Germany
E-mail: stefanie.rechberger@fau.de; erdmann.spiecker@fau.de

Dr. S. Rechberger, Dr. N. Gasparini, Prof. C. J. Brabec, Dr. T. Ameri
Institute of Materials for Electronics and Energy Technology
Friedrich-Alexander University Erlangen-Nuremberg
Martensstraße 7, 91058 Erlangen, Germany
E-mail: tayebeh.ameri@lmu.de

Dr. R. Singh, Dr. M. Kim, Prof. K. Cho
Department of Chemical Engineering
Pohang University of Science and Technology
Pohang 37673, Korea

Dr. R. Singh
Department of Energy Materials and Engineering
Dongguk University
Seoul 04620, Korea

Dr. C. L. Chochos
Advent Technologies SA
Stadiou Street, Platani, Rio, Patras 26504, Greece

Dr. C. L. Chochos
Institute of Chemical Biology
National Hellenic Research Foundation
48 Vassileos Constantinou Avenue, Athens 11635, Greece

Dr. V. G. Gregoriou
National Hellenic Research Foundation
48 Vassileos Constantinou Avenue, Athens 11635, Greece

Prof. C. J. Brabec
Research Department of High Throughput Methods in Photovoltaics
Helmholtz Institute Erlangen-Nürnberg for Renewable Energy
Immerwahrstraße 2
91058 Erlangen, Germany

Dr. T. Ameri
Chair of Physical Chemistry – Physical Chemistry and Nanoscience
Department of Chemistry
University of Munich (LMU)
Butenandtstrasse 5-13 (E), 81377 Munich, Germany

and thus increase the light harvesting, and one electron-acceptor material retaining the advantage of a single-junction device structure. Incorporating the third component changes the photophysics significantly in comparison with the reference binary BHJ solar cell. Fundamental principles such as charge transfer, energy transfer, and parallel linkage or alloy structure are closely related to the location of the third component in the ternary active layer. Therefore, the knowledge of the nanoscale morphology of the active layer is indispensable to understand and further improve the PCE.

Various characterization techniques are established to determine the morphology and structure of organic BHJ solar cells to elucidate morphology–performance relationships.[3] Some of these characterization techniques in real space (imaging) and reciprocal space (diffraction, scattering) were applied to ternary organic BHJ solar cells.[4] However, the successful determination of the material distribution for all three components has not been reported yet. Real-space techniques are essential to reveal the morphology in terms of the location and shape of individual domains and the material distribution. Reciprocal-space techniques offer additional information about the crystallinity, molecular order, and domain spacings. Transmission electron microscopy (TEM) is frequently used to visualize the morphology in real space with high spatial resolution. However, due to the similarity of involved polymers regarding chemical composition and electron densities, it was not possible so far to determine the material distribution of all three components.[2b,4c,e,f,l] Analytical TEM and especially energy-filtered TEM (EFTEM) provide rich additional information due to their chemical sensitivity and the ability to map differences in the electronic structure of involved materials.[3a,4g,h,5] Nevertheless, even with EFTEM the morphology determination of ternary organic BHJ solar cells remains a challenging task, in particular in cases where the two polymers show little differences with respect to their chemical composition and electronic structure represented in similar plasmonic energies.[4a,g,h,j,k] Here, we present the successful determination of the material distribution of all three components of a ternary organic BHJ solar cell using analytical TEM, which is, to the best of our knowledge, the first demonstration of its kind so far. We reveal the lateral as well as the cross-sectional morphology and the influence of different sensitizer concentrations on the morphology of the active layer, and correlate the morphology to the device performance.

In this work, the ternary organic BHJ solar cell based on the host system of indacenodithieno[3,2-b]thiophene, 2,3-bis(3-(octyloxy)phenyl)quinoxaline (PIDTTQ)[6] and [6,6]-phenyl C$_{70}$ butyric acid methyl ester (PC$_{70}$BM) incorporating the sensitizer poly[(4,4′-bis(2-ethylhexyl)dithieno[3,2-b:2′,3′-d]silole)-2,6-diylalt-(4,7-bis(2-thienyl)-2,1,3-benzothiadiazole)-5,5′-diyl] (Si-PCPDTBT)[7] is studied (Figure S1, Supporting Information). The extensive optoelectronic characterization of this system was reported in the publication of Gasparini et al.[8] A clear manifestation of a sensitization effect was demonstrated by incorporating Si-PCPDTBT into a PIDTTQ:PC$_{70}$BM host blend, changing fundamental photovoltaic processes in comparison with the binary system. The ternary blend shows lower performance under 1 sun condition in comparison with the binary blend, but delivers 6.1% PCE at 0.01 sun, clearly surpassing the best efficiency of the binary host blend due to the suppression of trap-assisted recombination. The reason for the low performance under 1 sun condition is attributed to the morphology of the active layer, which is presented here in detail.

2. Results and Discussion

EFTEM is an imaging technique based on inelastic scattering of electrons, where only electrons with specific energies are used to form the image.[9] For EFTEM investigations of a ternary BHJ layer, we combine three concepts using different information: 1) the elemental information, 2) the plasmonic information, and 3) pre-carbon imaging. **Figure 1** shows the EFTEM characterization of the ternary organic BHJ film PIDTTQ:Si-PCPDTBT:PC$_{70}$BM with a mixing ratio of 0.5:0.5:2 by weight.

Zero-loss (ZL)-filtered bright field (BF) imaging enhances the image contrast and resolution in comparison with BF imaging, as inelastically scattered electrons are filtered out. However, since ZL-filtered imaging only uses elastically scattered electrons, direct chemical information and information about the electronic structure of the material is lost. As a result, the identification and differentiation of PIDTTQ and Si-PCPDTBT is not possible. The dark domains shown in Figure 1a correspond to PC$_{70}$BM, which forms nanocrystals[10] that scatter the electrons in larger angles than the used objective aperture resulting in the dark contrast. In addition, black nanoparticles can be seen in the ternary film in the ZL-filtered BF image (Figure 1a). These nanoparticles were characterized by energy-dispersive X-ray spectroscopy (EDXS) (Figure S2, Supporting Information) revealing palladium and tin content. The nanoparticles originate from the synthesis of Si-PCPDTBT and were not removed completely in the scavenging and soxhlet extraction process.

To identify all three components and determine the nanomorphology, we utilize the differences in the chemical composition being directly proportional to the intensity values in elemental maps. The nominal chemical compositions of PIDTTQ, Si-PCPDTBT, and PC$_{70}$BM are shown in **Table 1** in atomic percent. All elemental maps shown in this work are based on EFTEM imaging and are determined using the three-window method.[9a,11] Figure 1b,c shows the elemental maps of sulfur and carbon using the S L$_{2,3}$ edge at an energy loss of 165 eV and the C K edge at 284 eV. The signals of N and O at energy losses of 401 and 532 eV, respectively, were too small to be used for EFTEM imaging. Furthermore, the Si L-edge signal at 99 eV originating entirely from Si-PCPDTBT was too small for EFTEM imaging due to the close proximity to the intense plasmon peak. Due to the difference of the carbon content of PC$_{70}$BM by a factor of 2 in comparison with PIDTTQ and Si-PCPDTBT, the elemental map of carbon can be used to represent PC$_{70}$BM. The carbon distribution (Figure 1c) confirms that the large domains already revealed in the ZL-filtered BF image (Figure 1a) are PC$_{70}$BM domains. In addition, dark fibers inside the PC$_{70}$BM domains are detected that are attributed to a polymer. Both polymers contain sulfur, whereby Si-PCPDTBT contains more than double the amount than PIDTTQ. In the elemental map of sulfur (Figure 1b), three intensity levels can be seen: a dark contrast representing the PC$_{70}$BM domains, a medium contrast indicating the matrix around the fullerene domains, and a bright fiber contrast. With respect to the composition of the polymers, the matrix is identified as PIDTTQ and the fibers as
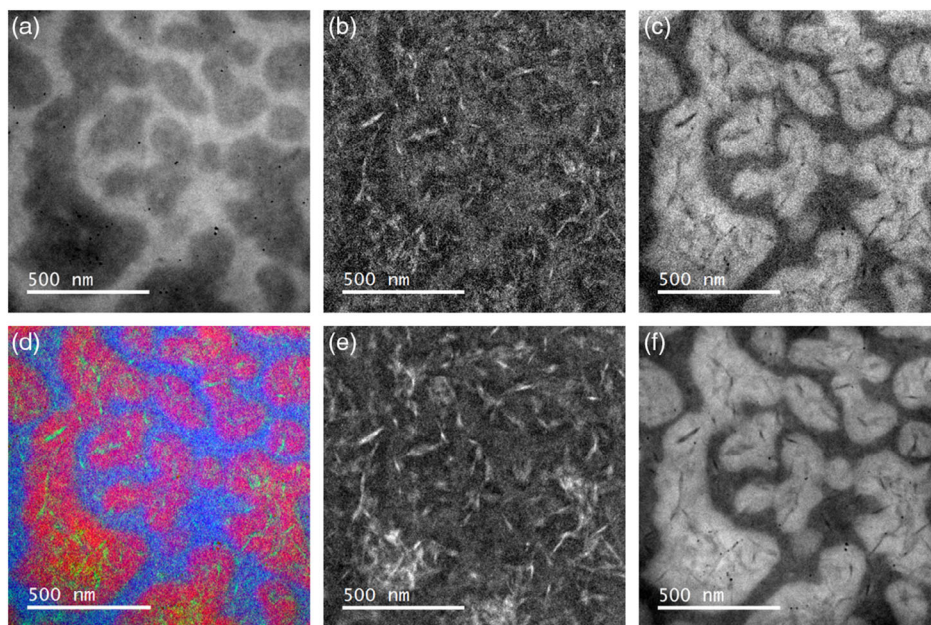
2000114 (2 of 8)

Figure 1. EFTEM characterization of the ternary film. a) ZL-filtered BF image, b) elemental map of sulfur using the S $L_{2,3}$ edge, c) elemental map of carbon using the C K edge, d) RGB color overlay representing the three materials (PIDTTQ: blue, Si-PCPDTBT: green, and PC$_{70}$BM: red), e) pre-carbon image at 267 ± 15 eV, and f) plasmon image at 30 ± 4 eV of PIDTTQ:Si-PCPDTBT:PC$_{70}$BM (0.5:0.5:2).

Table 1. Nominal composition of the organic materials used in the ternary BHJ solar cell.

Element	PIDTTQ [at%]	Si-PCPDTBT [at%]	PC$_{70}$BM [at%]
H	50.9	51.4	14.3
C	45.6	40.5	83.7
N	0.9	2.7	–
O	0.9	–	2.0
Si	–	1.4	–
S	1.8	4.1	–

Si-PCPDTBT. As the signals of sulfur of only 1.8 and 4.1 at% are relatively weak, we performed plasmon imaging and pre-carbon imaging to confirm these findings. Pre-carbon imaging uses electrons with an energy loss just below the carbon K edge. This effectively minimizes the contribution of carbon to the image and thus structures containing elements with lower-lying edges, such as sulfur, appear bright in the image.[9a] Figure 1e shows the pre-carbon image at an energy loss of 267 eV with an energy window of 30 eV, which maximizes the structure-sensitive contrast. The pre-carbon image confirms the findings about the material distribution and displays the polymer fibers at high spatial resolution. In addition to the ternary film, the pure materials were analyzed using electron energy-loss spectroscopy (EELS) to characterize the materials. Figure S3, Supporting Information, shows the EEL spectra of the low-loss region of PIDTTQ, Si-PCPDTBT, and PC$_{70}$BM. The broad peaks arising from collective oscillations of valence electrons are the plasmon peaks for the various materials. Noteworthy is also the π–π^* electronic transition of PC$_{70}$BM at 6 eV.[12] The plasmon peaks were fitted using Gaussian

functions leading to plasmon energies for the pure materials of 21.8 eV (PIDTTQ), 21.9 eV (Si-PCPDTBT), and 24.5 eV (PC$_{70}$BM). Both PIDTTQ and Si-PCPDTBT feature similar plasmon energies, whereas PC$_{70}$BM can clearly be distinguished. Thus, an EFTEM image at an energy loss of 30 ± 8 eV was acquired to differentiate between fullerene and polymers (Figure 1f). In this energy region, the contribution of PC$_{70}$BM dominates the contrast; therefore, the plasmon image at 30 eV represents PC$_{70}$BM. The plasmon image is in good agreement with the elemental map of carbon and shows the distribution of PC$_{70}$BM-rich domains with improved signal-to-noise ratio.

In summary, the PC$_{70}$BM-rich domains are consistently identified using the elemental map of carbon and the plasmon image at 30 eV. The domains extend over several hundreds of nanometers and contain narrow polymer fibers. The elemental map of sulfur and the pre-carbon image representing the polymers are in good agreement and complementary to the fullerene-representing images. The polymer-rich matrix surrounding the fullerene domains are assigned to PIDTTQ whereas the fibers preferentially contained in the fullerene domains are clearly identified as Si-PCPDTBT. In the case of a polymer mixing ratio of 0.5:0.5, the Si-PCPDTBT fibers are not fully contained in the fullerene domains but also occur in the polymer-rich matrix and even sometimes cross the interface between polymer matrix and fullerene domains. To visualize the nanomorphology of the ternary system, a RGB color overlay representing the three materials is shown in Figure 1d. In this figure, the ZL-filtered BF image colored in blue represents PIDTTQ, the elemental map of sulfur colored in green represents Si-PCPDTBT, and the elemental map of carbon colored in red represents PC$_{70}$BM.

To take advantage of the unique elemental characteristic of Si-PCPDTBT being the Si content, EDXS analysis focusing on
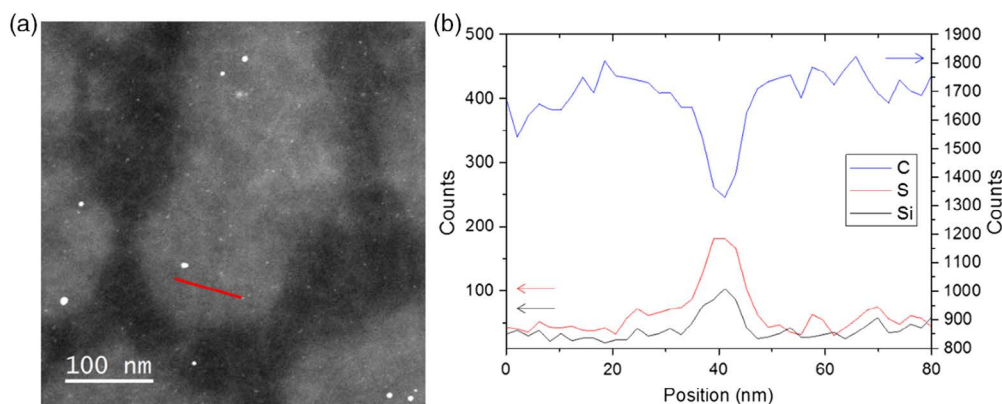
Figure 2. STEM EDXS line scan across a sensitizer fiber. a) STEM HAADF image of the ternary film with indicated line scan and b) EDXS line profile for carbon, sulfur, and silicon along the line in part (a) showing clearly the changes in the composition at the location of the Si-PCPDTBT fiber.

the Si K peak was performed. **Figure 2**a shows a scanning TEM (STEM) image taken in high-angle annular dark field (HAADF) mode basically resulting in inverted contrast with respect to the BF image in Figure 1a. Along the indicated line, an EDXS line scan was performed and the results for Si, S, and C are shown in Figure 2b. The line scan was placed in a $PC_{70}BM$-rich domain crossing a polymer fiber which appears only with weak contrast in HAADF-STEM image due to the lack of direct chemical information. However, from the EDXS line scan, the polymer fiber can be clearly identified as Si-PCPDTBT as the Si and S signals increase and the C signal decreases at the position of the fiber.

With this additional proof, the nanomorphology of the ternary organic BHJ active layer could be successfully elucidated using analytical TEM.

To investigate the influence of the third component on the nanomorphology of the ternary film, different PIDTTQ: Si-PCPDTBT weight ratios were studied. **Figure 3** shows the EFTEM characterization of ternary films with mixing ratios of $PIDTTQ:Si-PCPDTBT:PC_{70}BM$ of 0.75:0.25:2 (Figure 3a–e), 0.85:0.15:2 (Figure 3f–j), and 0.95:0.05:2 (Figure 3k–o). The images can be interpreted with the same contrast mechanisms as in Figure 1. Thus, the elemental maps of sulfur using the
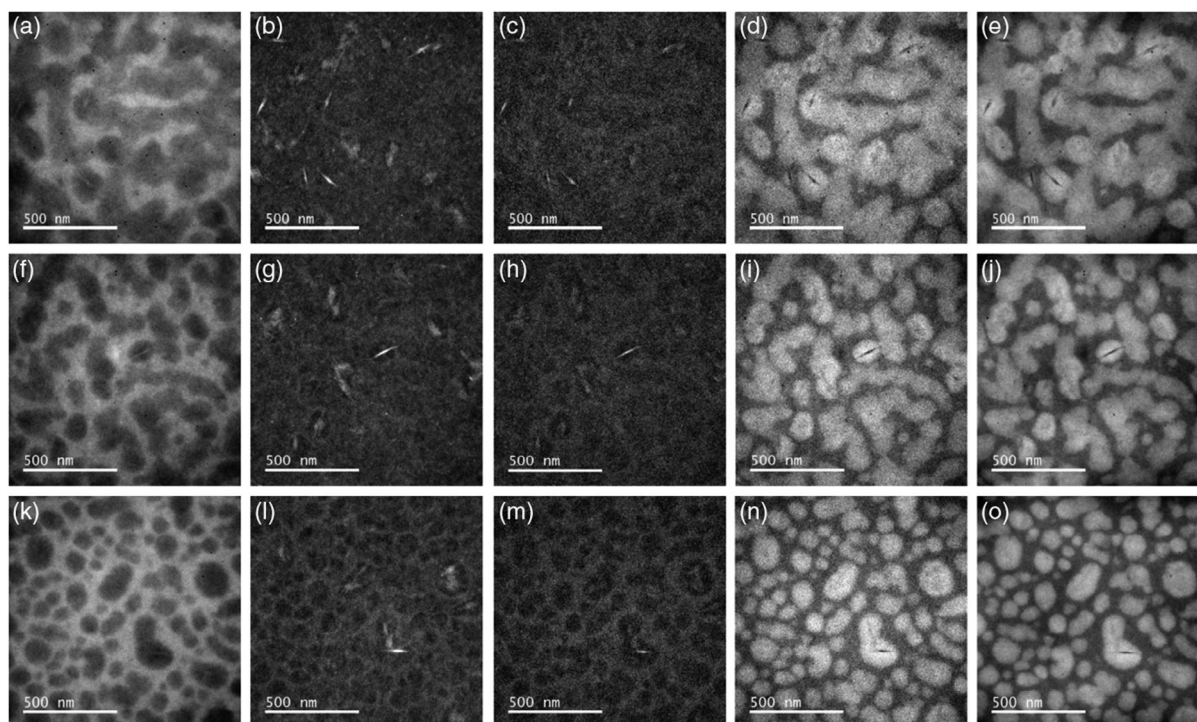

Figure 3. EFTEM characterization of the ternary film with different polymer to sensitizer concentrations. $PIDTTQ:Si-PCPDTBT:PC_{70}BM$ with mixing ratios of a–e) 0.75:0.25:2, f–j) 0.85:0.15:2, and k–o) 0.95:0.05:2. a,f,k) ZL-filtered BF images, b,g,l) pre-carbon images at 267 ± 15 eV, c,h,m) elemental maps of sulfur using the S $L_{2,3}$ edge, d,i,n) elemental maps of carbon using the C K edge, and e,j,o) plasmon images at 30 ± 4 eV.

S $L_{2,3}$ edge (Figure 3c,h,m) and the pre-carbon images at 267 ± 15 eV (Figure 3b,g,l) reveal the polymers with bright contrast, whereas the fullerene-rich domains appear bright in the elemental maps of carbon using the C K edge (Figure 3 d,i,n) and the plasmon images taken at an energy loss of 30 ± 4 eV (Figure 3e,j,o). To facilitate the comparison of the films with varying amount of sensitizer, all EFTEM images shown in Figure 1 and 3 were acquired at the same magnification. The morphology of the binary PIDTTQ:PC$_{70}$BM BHJ host blend containing PIDTTQ-MMW with medium molecular weight was already described by Gasparini et al.[6] In this case, separated domains with PC$_{70}$BM domain sizes of about 50 nm are formed. Upon adding sensitizer and successively increase the sensitizer amount, the PC$_{70}$BM domain sizes increase drastically to about 100 nm in the case of only 5% Si-PCPDTBT and further to several hundreds of nanometers and even micrometers in the case of 50% Si-PCPDTBT (Figure 1). For all mixing ratios, PIDTTQ constitutes the matrix in which the fullerene-rich domains are embedded, whereas Si-PCPDTBT forms fibers with lengths between 70 and 150 nm and diameters of about 10 nm. In the case of 50% sensitizer, the Si-PCPDTBT fibers occur in both domains, PC$_{70}$BM and PIDTTQ, as well as at the interfaces stretching from fullerene to polymer domains. Reducing the amount of Si-PCPDTBT reduces the number of Si-PCPDTBT fibers and reveals a preferential formation of the Si-PCPDTBT fibers in the PC$_{70}$BM domains.

As a complementary characterization technique, 2D grazing incidence wide-angle X-ray scattering (GIWAXS) was used to obtain insights into the molecular packing, orientation and crystallinity of the ternary organic BHJ active layers. Films of pure PIDTTQ polymer, binary host blend PIDTTQ:PC$_{70}$BM (1:2) and ternary blends PIDTTQ:Si-PCPDTBT:PC$_{70}$BM having 15% and 50% sensitizer were investigated and corresponding 2D GIWAXS patterns are shown in Figure S4, Supporting Information. The extracted structural data are presented in Table S1 and S2, Supporting Information, for the polymers and PC$_{70}$BM, respectively. In addition, schemes of the idealized unit cells of PIDTTQ and Si-PCPDTBT are presented in Figure S5, Supporting Information. The 2D GIWAXS pattern of pure PIDTTQ shows an in-plane reflection at $q_{xy} = 0.34\,\text{Å}^{-1}$ (d-spacing $= 18.5$ Å), which relates to the backbone repeat (001) diffraction of PIDTTQ crystals.[13] A broad out-of-plane reflection was also observed at $q_z = 1.39\,\text{Å}^{-1}$ (d-spacing $= 4.5$ Å), which is indexed by $\pi-\pi$ stacking (010) reflection. The in-plane (001) and broad out-of-plane reflection suggests that planes of PIDTTQ aromatic backbones are roughly aligned parallel to the surface plane of the substrate known as "face-on" orientation, as shown in Figure S5, Supporting Information. In the 2D GIWAXS pattern of the PIDTTQ:PC$_{70}$BM (1:2) blend film, the (001) backbone diffraction peak indicates that the polymer component still maintains the face-on orientation with a coherence length of 7.6 nm. In the ternary blend, an increase in the coherence length of PIDTTQ to 9.3 nm for the blend having 15% Si-PCPDTBT sensitizer has been observed. It increases further to 15.6 nm for 50% of Si-PCPDTBT. In the ternary blend, two additional out-of-plane peaks at $q_z = 0.36\,\text{Å}^{-1}$ and $q_z = 1.77\,\text{Å}^{-1}$ occur, which can be attributed to the Si-PCPDTBT sensitizer. The peak at $q_z = 0.36\,\text{Å}^{-1}$ (d-spacing $= 17.5$ Å) corresponds to the spacing between adjacent chains set by the branched side

chains.[14] The broad peak at $q_z = 1.78\,\text{Å}^{-1}$ (d-spacing $= 3.5$ Å) represents $\pi-\pi$ stacking between the backbone of the Si-PCPDTBT polymer. Based on the comparison of the alkyl chain stacking peaks (at $q_z = 0.36\,\text{Å}^{-1}$) of in-plane and out-of-plane profiles, Si-PCPDTBT exhibits bimodal orientation of backbones having both edge-on and face-on orientations. Moreover, the stronger $\pi-\pi$ stacking peak of Si-PCPDTBT in the out-of-plane scattering geometry means that the face-on orientation is more dominant than the edge-on orientation in the blend films, which is preferential for vertical charge transport.[15]

The cross-sectional morphology is a further important aspect as it strongly influences the device performance by defining the percolation pathways of the charges to the electrodes. To get information about the cross-sectional morphology, a cross-section of the whole solar cell was prepared using the in situ lift-out technique in a scanning electron microscope/focused ion beam (SEM/FIB) dual beam system. **Figure 4** shows the EFTEM characterization of two different areas of the cross-section of the ternary organic BHJ solar cell with a mixing ratio of 0.5:0.5:2 for PIDTTQ:Si-PCPDTBT:PC$_{70}$BM. The ZL-filtered BF images (Figure 4a,f) clearly reveal the vertical layer stacking of the solar cell, comprising layers of indium tin oxide (ITO) and ZnO below the active BHJ layer and MoO$_x$ and Ag layers above. The cross-sectional morphology of the active layer is characterized using elemental maps of sulfur (Figure 4c,h) and carbon (Figure 4d,i) as well as pre-carbon images (Figure 4b,g) and the plasmon images at 30 ± 4 eV (Figure 4e,j). Again, the EFTEM images can be interpreted using the contrast mechanisms discussed in detail in connection with Figure 1, thus enabling the discrimination of the two polymer phases and the fullerene derivative. The key information that can be extracted from the cross-sectional images is the relative location of the Si-PCPDTBT fibers with respect to the PC$_{70}$BM domains in vertical direction. This information is not accessible from plan-view TEM images (Figure 1–3) which represent projections through the thickness of the film, thus making it impossible to discriminate whether the Si-PCPDTBT fibers are located above, below, or inside the PC$_{70}$BM domains. In the first cross-sectional area shown in Figure 4a–e, PC$_{70}$BM forms circular and circular-segmented shapes and PIDTTQ-rich domains fill the space in between. Si-PCPDTBT fibers (marked with white arrows) are located in the PC$_{70}$BM rich domain; in addition, one fiber in the middle of the images stretches into the PIDTTQ-rich domain. In Figure 4f–j, one Si-PCPDTBT fiber that formed along the interface of PC$_{70}$BM and PIDTTQ domains is shown. Furthermore, circular cross-sections of two sensitizer fibers can be seen in Figure 4f–j, as the orientation of the fibers are in this case perpendicular to the lamella of the solar cell. One of these Si-PCPDTBT fibers is located within the PIDTTQ-rich domain, whereas the other is located in the middle of the PC$_{70}$BM rich domain. With these results, the nanomorphology of this ternary organic solar cell is fully elucidated, revealing the formation of Si-PCPDTBT fibers inside both, PIDTTQ and PC$_{70}$BM domains, as well as at their interfaces.

In addition to the morphological aspects, we now turn our attention to the photophysical behavior of studied blends in organic solar devices. Recently, we have shown that blending PIDTTQ and Si-PCPDTBT at equal weight ratio (PIDTTQ:Si-PCPDTBT:PC$_{70}$BM 0.5:0.5:2) changes the charge recombination order of the binary PIDTTQ:PC$_{70}$BM, resulting in reduced
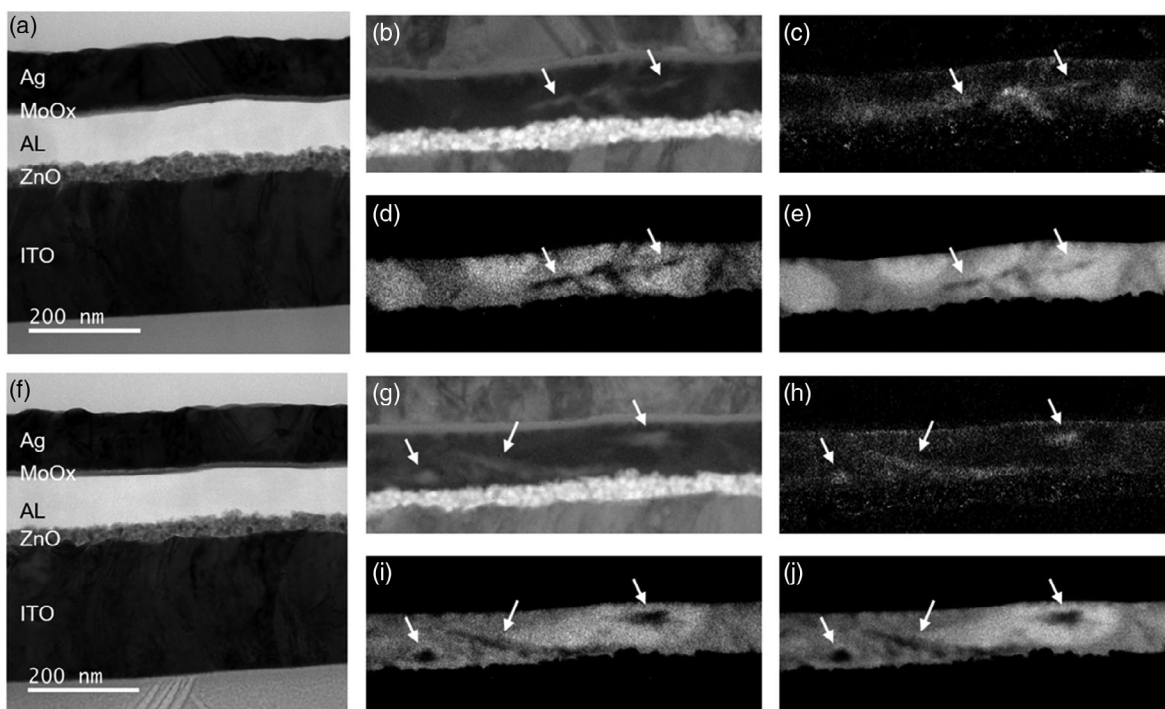
Figure 4. EFTEM characterization of the cross-section of the ternary organic solar cell. a,f) ZL-filtered BF images of all layers of the solar cell (ITO/ZnO/active layer: PIDTTQ:Si-PCPDTBT:PC$_{70}$BM/MoO$_x$/Ag). b,g) Pre-carbon images at 267 ± 15 eV, c,h) elemental maps of sulfur using the S L$_{2,3}$ edge, d,i) elemental maps of carbon using the C K edge, and e,j) plasmon images at 30 ± 4 eV of the active layer. White arrows indicate Si-PCPDTBT fibers.

trap-assisted recombination in the ternary blends. This leads to a PCE in the excess of 6% at low light intensity (1 mW cm^{-2}), compared with the limited performances of reference binary devices (PCE = 2%).[8] Our analytical TEM analyses revealed that Si-PCPDTBT fibers are preferentially located in PC$_{70}$BM-rich domains; therefore, to disentangle the effect of the third component, we fabricate binary devices based on Si-PCPDTBT:PC$_{70}$BM at different donor to acceptor (D/A) ratios and study the current–voltage ($J–V$) characteristics at different light levels. The $J–V$ curves and the photovoltaic parameters of the solar cells are shown in Figure S6 and Table S3, Supporting Information, respectively. We found that by decreasing the amount of donor polymer the PCE is reduced from 1:1 to 0.125:1 D:A due to a reduced light harvesting capability of the photoactive layer. Figure S7, Supporting Information, shows the open-circuit voltage (V_{OC}) as function of light intensity for Si-PCPDTBT:PC$_{70}$BM devices. The light-intensity dependence of the V_{OC} directly provides insight into the role of trap-assisted recombination versus second-order recombination at the open-circuit condition. Although, for second-order recombination, the slope of V_{OC} versus ln(P_{in}) is equal to kT/q, the presence of additional mechanism of trap-assisted recombination results in a stronger dependency of V_{oc} on the light intensity reflected by a slope of $2kT/q$.[16] As shown in Figure S6, Supporting Information, we find that the contribution of trap-assisted recombination increases upon increasing the amount of donor material, reflected by a slope of 1.06, 1.08, 1.12, and 1.23 kT/q for Si-PCDTBT:PC$_{70}$BM ratios of 0.125:1, 0.25:1, 0.5:1, and 1:1, respectively. Importantly, comparison with the ternary blends shows that, for a PIDTTQ:Si-PCPDTBT:PC$_{70}$BM

ratio of 0.50:0.50:2, the same slope is observed as for the binary Si-PCPDTBT:PC$_{70}$BM with ratio 0.25:1, suggesting that small addition of Si-PCPDTBT leads to a reduced trap assisted recombination. However, the Si-PCPDTBT mix in PIDTTQ at high loading of the third component causes bimolecular recombination as well as coarsening of the morphology. The overoptimized size of fullerene domains, formed by introducing Si-PCPDTBT into the host system, hinders the continuous percolation pathway for electrons and causes another source of bimolecular recombination. As a result, a significant improvement of ≈60% in PCE is observed for ternary organic solar cells at low light levels, where the bimolecular recombination is negligible and trap-assisted recombination is suppressed due to the specific nanomorphology formed by introducing Si-PCPDTBT polymer into the PIDTTQ:PC$_{70}$BM host system. For further details on solar devices performance and characterization, we refer to the publication of Gasparini et al.[8]

3. Conclusion

In summary, we successfully elucidated the nanomorphology of a ternary organic solar cell using multimodal analytical TEM and correlated it to the device performance. By combining high-resolution imaging with analytical techniques such as EELS and EFTEM at various energy losses as well as EDXS, the material distribution of all three organic components in the BHJ active layer was determined. The impact of the sensitizer polymer Si-PCPDTBT on the nanomorphology of the PIDTTQ:PC$_{70}$BM

blend as well as the phase formation was demonstrated by investigating various mixing ratios of the polymers and the cross-sectional morphology of the solar cell. It could be shown that the size of the $PC_{70}BM$ domains depends on the amount of Si-PCPDTBT, which forms fibers, located preferentially in the $PC_{70}BM$ domains. At high sensitizer contents, the Si-PCPDTBT fibers additionally form in the PIDTTQ-rich domains as well as at the PIDTTQ:$PC_{70}BM$ interfaces. Revealing the nanomorphology of these ternary organic solar cells leads to a better understanding of the device performance of the ternary system in comparison with the binary reference illuminated under 1 sun as well as under low light intensities. It could be demonstrated that analytical TEM is a powerful toolset to reveal the morphology of ternary organic solar cells for all involved components and elucidate the morphology/device performance relation to further improve the capabilities of OPV.

4. Experimental Section

Device Fabrication: All devices were fabricated using doctor-blading under ambient conditions. The active layer films for TEM investigations were deposited on poly(3,4-ethylenedioxythiophene) polystyrene sulfonate (PEDOT:PSS) (50 nm)-coated glass. The active layers consisted of PIDTTQ:Si-PCPDTBT:$PC_{70}BM$ (20 g L^{-1} in a mixture of 1,2-dichlorobenzene [o-DCB] and 1-chloronaphthalene [CN] 97 to 3 vol%). The amount of Si-PCPDTBT and PIDTTQ was varied, whereas the overall polymer-to-fullerene ratio was kept at 1:2 by weight.

The BHJ solar cells were fabricated in inverted device configuration with the structure ITO/ZnO/active layer/MoO_x/Ag. Therefore, prestructured ITO substrates were cleaned with acetone and isopropyl alcohol in an ultrasonic bath for 10 min each. After drying, the substrates were coated by doctor-blading with zinc oxide (ZnO) and the active layer based on PIDTTQ:Si-PCPDTBT:$PC_{70}BM$. MoO_x and Ag were thermally evaporated through a mask under a vacuum of $\approx 2 \times 10^{-6}$ mbar.

TEM: Analytical TEM investigations were performed using an FEI Titan Themis^3 300 TEM equipped with a high-brightness field-emission gun (X-FEG) operated at 200 kV. It was equipped with a high-resolution Gatan Imaging Filter (GIF Quantum) used for EELS as well as energy-filtered TEM (EFTEM) and a four-quadrant silicon drift detector (SDD) system (Super-X detector) used for EDXS. In addition, the TEM was equipped with a probe Cs corrector and an image Cs corrector as well as a monochromator.

The active layer films for the TEM investigations were prepared as plan-view specimens. Therefore, the doctor-bladed sample was put into a vessel containing distilled water to float off the active layer. As PEDOT:PSS dissolved in the water, the active layer film was transferred to a lacey carbon film TEM supporting grid.

The cross-section samples were prepared using a SEM/FIB DualBeam system, an FEI Helios NanoLab 660. The in situ lift-out technique was chosen to realize homogeneously thin cross-section lamellas. To protect the surface from beam damage, carbon layers were grown by electron-beam-induced deposition followed by ion-beam-assisted deposition.

GIWAXS: GIWAXS measurements were performed at 3C and 9A beamlines at Pohang Accelerator Laboratory (PAL). The photon energy was 10.2502 keV ($\lambda = 1.2095$ Å). The angle between the film surface and the incident beam was fixed at 0.13° for all samples. The 2D GIWAXS images from the films were analyzed according to the relationship between the scattering vector $\mathbf{q}$ and the d spacing, $\mathbf{q} = 2\pi/d$. The GIWAXS images shown are normalized with respect to the exposure time.

Supporting Information

Supporting Information is available from the Wiley Online Library or from the author.

Conflict of Interest

The authors declare no conflict of interest.

[1] a) L. Lu, T. Zheng, Q. Wu, A. M. Schneider, D. Zhao, L. Yu, *Chem. Rev.* **2015**, *115*, 12666; b) H. Li, Z. Xiao, L. Ding, J. Wang, *Sci. Bull.* **2018**, *63*, 340; c) L. Meng, Y. Zhang, X. Wan, C. Li, X. Zhang, Y. Wang, X. Ke, Z. Xiao, L. Ding, R. Xia, H.-L. Yip, Y. Cao, Y. Chen, *Science* **2018**, *361*, 1094; d) J. Zhang, L. Zhu, Z. Wei, *Small Methods* **2017**, *1*, 1700258.

[2] a) T. Ameri, P. Khoram, J. Min, C. J. Brabec, *Adv. Mater.* **2013**, *25*, 4245; b) L. Lu, M. A. Kelly, W. You, L. Yu, *Nat. Photonics* **2015**, *9*, 491; c) Q. An, F. Zhang, J. Zhang, W. Tang, Z. Deng, B. Hu, *Energy Environ. Sci.* **2016**, *9*, 281; d) W. Huang, P. Cheng, Y. Yang, G. Li, Y. Yang, *Adv. Mater.* **2018**, *30*, 1705706.

[3] a) D. M. Delongchamp, R. J. Kline, A. Herzing, *Energy Environ. Sci.* **2012**, *5*, 5980; b) F. Liu, Y. Gu, X. Shen, S. Ferdous, H.-W. Wang, T. P. Russell, *Prog. Polym. Sci.* **2013**, *38*, 1990; c) Y. Huang, E. J. Kramer, A. J. Heeger, G. C. Bazan, *Chem. Rev.* **2014**, *114*, 7006.

[4] a) Y. Gu, C. Wang, F. Liu, J. Chen, O. E. Dyck, G. Duscher, T. P. Russell, *Energy Environ. Sci.* **2014**, *7*, 3782; b) L. Lu, T. Xu, W. Chen, E. S. Landry, L. Yu, *Nat. Photonics* **2014**, *8*, 716; c) J. Fang, Z. Wang, J. Zhang, Y. Zhang, D. Deng, Z. Wang, K. Lu, W. Ma, Z. Wei, *Adv. Sci.* **2015**, *2*, 1500250; d) L. Lu, W. Chen, T. Xu, L. Yu, *Nat. Commun.* **2015**, *6*, 7327; e) J. Zhang, Y. Zhang, J. Fang, K. Lu, Z. Wang, W. Ma, Z. Wei, *J. Am. Chem. Soc.* **2015**, *137*, 8176; f) Y. Zhang, D. Deng, K. Lu, J. Zhang, B. Xia, Y. Zhao, J. Fang, Z. Wei, *Adv. Mater.* **2015**, *27*, 1071; g) N. Gasparini, X. Jiao, T. Heumueller, D. Baran, G. J. Matt, S. Fladischer, E. Spiecker, H. Ade, C. J. Brabec, T. Ameri, *Nat. Energy* **2016**, *1*, 16118; h) L. Ke, J. Min, M. Adam, N. Gasparini, Y. Hou, J. D. Perea, W. Chen, H. Zhang, S. Fladischer, A. C. Sale, E. Spiecker, R. R. Tykwinski, C. J. Brabec, T. Ameri, *Adv. Energy Mater.* **2016**, *6*, 1502355; i) Z. Wang, Y. Zhang, J. Zhang, Z. Wei, W. Ma, *Adv. Energy Mater.* **2016**, *6*, 1502456; j) X. Du, X. Jiao, S. Rechberger, J. D. Perea, M. Meyer, N. Kazerouni, E. Spiecker, H. Ade, C. J. Brabec, R. H. Fink, T. Ameri, *Macromolecules* **2017**, *50*, 2415; k) L. Ke, N. Gasparini, J. Min, H. Zhang, M. Adam, S. Rechberger, K. Forberich, C. Zhang, E. Spiecker, R. R. Tykwinski, C. J. Brabec, T. Ameri, *J. Mater. Chem. A* **2017**, *5*, 2550; l) J. W. Lee, Y. S. Choi, H. Ahn, W. H. Jo, *ACS Appl. Mater. Inter.* **2016**, *8*, 10961; m) T. Ameri, P. Khoram, T. Heumüller, D. Baran, F. MacHui,

A. Troeger, V. Sgobba, D. M. Guldi, M. Halik, S. Rathgeber, U. Scherf, C. J. Brabec, *J. Mater. Chem. A* **2014**, *2*, 19461; n) N. Gasparini, S. Kahmann, M. Salvador, J. D. Perea, A. Sperlich, A. Baumann, N. Li, S. Rechberger, E. Spiecker, V. Dyakonov, G. Portale, M. A. Loi, C. J. Brabec, T. Ameri, *Adv. Energy Mater.* **2019**, *9*, 1803394.

[5] a) L. F. Drummy, R. J. Davis, D. L. Moore, M. Durstock, R. A. Vaia, J. W. P. Hsu, *Chem. Mater.* **2011**, *23*, 907; b) D. R. Kozub, K. Vakhshouri, L. M. Orme, C. Wang, A. Hexemer, E. D. Gomez, *Macromolecules* **2011**, *44*, 5722.

[6] N. Gasparini, A. Katsouras, M. I. Prodromidis, A. Avgeropoulos, D. Baran, M. Salvador, S. Fladischer, E. Spiecker, C. L. Chochos, T. Ameri, C. J. Brabec, *Adv. Funct. Mater.* **2015**, *25*, 4898.

[7] M. C. Scharber, M. Koppe, J. Gao, F. Cordella, M. A. Loi, P. Denk, M. Morana, H.-J. Egelhaaf, K. Forberich, G. Dennler, R. Gaudiana, D. Waller, Z. Zhu, X. Shi, C. J. Brabec, *Adv. Mater.* **2010**, *22*, 367.

[8] N. Gasparini, M. Salvador, S. Fladischer, A. Katsouras, A. Avgeropoulos, E. Spiecker, C. L. Chochos, C. J. Brabec, T. Ameri, *Adv. Energy Mater.* **2015**, *5*, 1501527.

[9] a) R. F. Egerton, *Electron Energy-Loss Spectroscopy in the Electron Microscope*, Springer, New York, NY, **2011**; b) D. B. Williams, C. B. Carter, *Transmission Electron Microscopy: A Textbook for Materials Science*, Springer, New York, NY, **2009**.

[10] X. Yang, J. K. J. van Duren, M. T. Rispens, J. C. Hummelen, R. A. J. Janssen, M. A. J. Michels, J. Loos, *Adv. Mater.* **2004**, *16*, 802.

[11] N. Bonnet, C. Colliex, C. Mory, M. Tence, *Scan. Microsc. Suppl.* **1988**, *2*, 351.

[12] E. E. Koch, A. Otto, *Opt. Commun.* **1969**, *1*, 47.

[13] C. L. Chochos, R. Singh, M. Kim, N. Gasparini, A. Katsouras, C. Kulshreshtha, V. G. Gregoriou, P. E. Keivanidis, T. Ameri, C. J. Brabec, K. Cho, A. Avgeropoulos, *Adv. Funct. Mater.* **2016**, *26*, 1840.

[14] M. Morana, H. Azimi, G. Dennler, H.-J. Egelhaaf, M. Scharber, K. Forberich, J. Hauch, R. Gaudiana, D. Waller, Z. Zhu, K. Hingerl, S. S. van Bavel, J. Loos, C. J. Brabec, *Adv. Funct. Mater.* **2010**, *20*, 1180.

[15] a) M.-H. Jao, H.-C. Liao, W.-F. Su, *J. Mater. Chem. A* **2016**, *4*, 5784; b) Z. Lin, Y. Yang, A. Zhang, *Polymer-Engineered Nanostructures for Advanced Energy Applications*, Springer, Switzerland **2017**.

[16] a) L. J. A. Koster, V. D. Mihailetchi, R. Ramaker, P. W. M. Blom, *Appl. Phys. Lett.* **2005**, *86*, 123509; b) A. K. K. Kyaw, D. H. Wang, V. Gupta, W. L. Leong, L. Ke, G. C. Bazan, A. J. Heeger, *ACS Nano* **2013**, *7*, 4569.

2000114 (8 of 8)